Magnetic ordering in Eu$_2$In and Eu$_2$Sn[☆]

C. Ritter [a,*], D.H. Ryan [b], A. Provino [c,d,f,**], G. Lamura [e], Y. Mudryk [d], R.K. Chouhan [d], P. Singh [d],
D.D. Johnson [d,e], V.K. Pecharsky [d,e], P. Manfrinetti [c,d,f]

[a] *Institut Laue-Langevin, BP 156, 38042, Grenoble, France*
[b] *Physics Department and Centre for the Physics of Materials, McGill University, 3600 University Street, Montreal, Quebec, Canada*
[c] *Department of Chemistry, University of Genova, Via Dodecaneso 31, Genova 16146, Italy*
[d] *Ames National Laboratory of US Department of Energy, Iowa State University, Ames, IA 50011, USA*
[e] *Department of Materials Science and Engineering, Iowa State University, Ames IA 50011, USA*
[f] *Institute SPIN-CNR, Corso Perrone 24, Genova 16152, Italy*

ARTICLE INFO

ABSTRACT

Eu$_2$In and Eu$_2$Sn crystallize in the orthorhombic Co$_2$Si-type structure (*oP*12, *Pnma*, No. 62) with In and Sn atoms occupying one 4*c* site and the Eu atoms filling two other 4*c* sites. Eu$_2$In has a nearly ideal first-order magnetostructural transition (FOMT) at 55 K with a hysteresis of less than 0.1 K, a large entropy change and an adiabatic temperature change of 5.0 K in a field of 2 T. The anhysteretic nature of the FOMT is likely due to there being no change in cell symmetry and relatively small changes in the lattice parameters. There is no magnetostructural transition in Eu$_2$Sn. Here we present the results of powder neutron diffraction, magnetization, and Eu Mössbauer spectroscopy aimed to investigate the nature of magnetic order for both Eu$_2$In and Eu$_2$Sn. The Eu Mössbauer spectrum of Eu$_2$In at 5 K shows two equal area components, consistent with Eu occupying two equal multiplicity crystallographic sites. However, the different hyperfine fields (B) of 27 T and 17 T suggest that the magnetic environments of the Eu moments on the two 4*c* sites are different. Neutron diffraction data at 2.5 K show that in Eu$_2$In the order is ferromagnetic, with Eu moments on both Eu sites oriented parallel to the *a*-axis; moment values of 6.8 μ$_B$ and 6.5 μ$_B$ were found. For Eu$_2$Sn measurements find two antiferromagnetic transitions, which are corroborated by neutron diffraction. Analysis of density-functional theory calculations shows negligible energy difference between differing magnetic configurations, indirectly supporting stability of multiple magnetic structures observed experimentally. While the transition at T$_{N1}$ = 30 K corresponds to the formation of a simple $k_1 = 0$ antiferromagnetic structure with Eu-moments pointing along the *b*-axis, at T$_{N2}$ = 13 K a coexisting second magnetic order with $k_2 = [0, ½, ½]$ appears.

1. Introduction

First-order phase transitions associated with changes in magnetic ordering are at the heart of developing advanced functional magnetocaloric materials [1–4]. Recently, the renewed interest in the environmentally-friendly hydrogen-fueled future brought the importance of hydrogen liquefaction and storage. Considering that the efficiency of magnetic cooling is much higher in the cryogenic range compared with the room temperature and magnetic rare earth (RE) compounds are optimal materials for cryogenic magnetic refrigeration, the RE compounds with large magnetocaloric effect in the cryogenic range are of notable impact. The discovery of giant magnetocaloric effect in Eu$_2$In [5] spurred significant attention to this and other RE$_2$In compounds, in particular to their fundamental behaviors [6–11]. In this regard, the interesting differences in magnetic properties of Eu$_2$In and Eu$_2$Sn have stimulated research on understanding their basic magnetism and its relationship with the electronic structure [12–14]. While Eu$_2$In was found to show a nearly ideal first-order magnetostructural transition from paramagnetic (PM) to ferromagnetic (FM) state at T$_C$ = 55 K, with hysteresis of less than 0.1 K, a large entropy change and an adiabatic temperature change of 5.0 K in a field of 2 T, the homolog Eu$_2$Sn was found to show a conventional second-order transition from PM to

antiferromagnetic (AFM) state at $T_N = 31$ K. In previous work, differences in local magnetic behavior between Eu$_2$In and Eu$_2$Sn were investigated using ^{151}Eu Mössbauer spectroscopy and band-structure calculations; it was found that the magnetic environments of Eu atoms in the two isostructural compounds are completely different [12]. Eu$_2$In exhibits two distinct Eu sites with hyperfine fields that differ by more than 50%. In contrast, the two sites are not resolved in Eu$_2$Sn and the observed hyperfine field is remarkably small [12]. The *ab initio* calculations of Eu$_2$In suggest that the interactions between $4f$ moments in this compound deviate from the standard RKKY model and the itinerant valence electrons have strong relevance to its first-order transition [13].

Eu$_2$In and Eu$_2$Sn both crystallize in the same orthorhombic Co$_2$Si-type structure [15] (*oP*12, *Pnma*, No. 62) that shows three inequivalent Wyckoff positions with 4c symmetry. In and Sn atoms occupy one of the 4c sites (occupied by Si atoms in the prototype) and the Eu atoms fill the two other 4c sites. Details and the structure can be found in the literature [5,12,16]. Eu$_2$In forms peritectically at 712 °C (Eu$_2$In → EuIn + L) [16] while Eu$_2$Sn forms congruently at 1355 °C (Eu$_2$Sn → L) [17].

Here we have investigated the magnetic structure of both Eu$_2$In and Eu$_2$Sn by neutron powder diffraction and studied the nature of the magnetic order occurring in Eu$_2$In on the Eu atoms in the two Wyckoff sites by Mössbauer spectroscopy. Neutron diffraction confirms the first-order magnetic transition in Eu$_2$In and shows that the order is ferromagnetic, with the Eu moments on both Eu sites oriented parallel to the a-axis, while the isostructural Eu$_2$Sn is shown to adopt a completely different antiferromagnetic order with the presence of two coexisting magnetic propagation vectors. In addition, density-functional theory (DFT) calculations were performed for various configurations, and we found that the Eu$_2$In structure supports a ferromagnetic state while, in contrast, Eu$_2$Sn supports an easy-axis-oriented antiferromagnetic (near collinear) state with similar magnetic moments for Eu sites to neutron diffraction, corroborating our experimental findings.

2. Experimental and Theoretical Details

2.1. Synthesis and phase characterization

Polycrystalline samples with nominal compositions Eu$_2$In and Eu$_2$Sn were prepared by induction melting using high-purity Eu from the Materials Preparation Center of the Ames Laboratory [18] and commercial grade In and Sn (99.999 wt% purity each). Due to air sensitivity of Eu and the final alloys, all the operations and handling of the elements and samples were carried out in a glove-box under pure Ar atmosphere. Total mass of the samples was 8–9 g. Pieces of each element for both samples were placed into an outgassed Ta crucible, which was sealed under flowing Ar. The samples were then melted in a high-frequency induction furnace under vacuum up to ≈ 1000 °C (Eu$_2$In) and ≈ 1350 °C (Eu$_2$Sn), shaking them to ensure homogenization [17]. The crucibles were sealed under vacuum in quartz tubes and annealed in a resistance furnace at 680 °C for 10 days (Eu$_2$In) and at 1000 °C for 11 days (Eu$_2$Sn). The samples then were slowly cooled down to room temperature. The final alloys show a gray metallic luster and are extremely air sensitive, with Eu$_2$Sn also being pyrophoric. Phase analysis was performed by X-ray powder diffraction using an X'Pert diffractometer (Cu Kα1 radiation). No extra phases were detected in the In samples, while small amounts of Eu$_5$Sn$_3$ and Eu$_2$O$_3$ (at a few vol% and trace amounts, respectively) were found in the Sn sample. The diffraction patterns were indexed with the aid of Lazy-PulveriX [19] and the lattice parameters were obtained by means of least-squares method. The X-ray analysis confirmed an orthorhombic Co$_2$Si-type (*oP*12, *Pnma*, No. 62) crystal structure for both compounds, with lattice parameters $a = 7.481(3)$ Å, $b = 5.586(3)$ Å, $c = 10.332(4)$ Å for Eu$_2$In and $a = 7.859(3)$ Å, $b = 5.403(4)$ Å, $c = 9.936(5)$ Å for Eu$_2$Sn (and unit-cell volumes of 431.76 and 421.90 Å^3, respectively).

2.2. DC magnetic susceptibility measurements

The temperature dependence of the dc magnetic susceptibility χ_m of Eu$_2$Sn was measured by using a commercial magnetometer (MPMS2 by Quantum Design). Several measurements in applied magnetic fields of 0.1, 1, 10 and 50 kOe were performed with both zero-field-cooled (ZFC) and field-cooled (FC) protocols. Such data let us determine the transition temperatures, their nature, and the Eu effective magnetic moment in the paramagnetic state (*vide infra*).

2.3. Neutron diffraction

The measurements on Eu$_2$In and Eu$_2$Sn were performed using neutrons with $\lambda = 2.4$ Å on the high intensity powder diffractometer D20, Institut Laue-Langevin, Grenoble, France. Due to the extremely high absorption cross section of Eu ($\sigma_{abs} = 4530$ b) the measurements had to use a special large-area sample holder with flat geometry [20]. Inside an argon-filled glove box the air-sensitive powder samples were placed onto a first Si plate, distributed evenly the best as possible, fixed with varnish, placed in an Al sample frame and covered with a second Si plate. The Al frame was closed, and the sample (after adjusting the length of the sample stick) was placed inside the cryostat where a pressure of about 80 mBar of He-gas exchange exists. The angle of the plate relative to the incoming neutron beam was optimised by measuring and turning the plate. Small changes of the angle have large influence on the existence of single crystal reflections from the Si plates. The Al peaks from the Al frame were mostly suppressed by some cadmium shielding. At about 45° relative to the beam the spectrum is best, showing a nearly featureless linear background and Bragg peaks of sufficient intensity. The beam was kept largely open to get maximum intensity on the plate. The thermal dependence of the diffraction pattern (thermodiffractogram) of Eu$_2$In was first measured recording a spectrum every 5 min while changing the temperature from 2.5 K to 65 K by 0.1 K every 20 s resulting in a temperature resolution of 1.5 K. Long data sets of 1.5 h were then taken at 2.5 K, 15 K, 30 K, 40 K, 50 K, 52 K, between 54 and 58 K every Kelvin and at 60 K. The thermodiffractogram of Eu$_2$Sn was measured between 2.5 K and 40 K with a ramp speed of 0.1 K/100 s. Data sets of 15 min were taken giving a temperature resolution of 0.9 K between data points. Long measurements of 5 h each were then made at 2.5 K, 19.5 K and 40 K. The neutron diffraction data were analyzed using the Rietveld refinement program FULLPROF [21], magnetic symmetry analysis was done using the program BASIREPS [22,23] and the program MAXMAGN which is part of the Bilbao Crystallographic Server [24,25].

2.4. Mössbauer spectroscopy

Samples were prepared for Mössbauer spectroscopy by hand grinding under hexane in a nitrogen-filled glove-box to reduce the possibility of oxidation. The ^{151}Eu Mössbauer spectroscopy measurements were carried out using a 4 GBq ^{151}SmF$_3$ source, driven in sine mode and calibrated using a standard 57CoRh/α-Fe foil. Isomer shifts are quoted relative to EuF$_3$ at ambient temperature. The 21.6 keV gamma rays were recorded using a thin NaI scintillation detector. The sample was cooled in a vibration-isolated closed-cycle helium refrigerator with the sample in a helium exchange gas. The spectra were fitted to a sum of Lorentzian lines with the positions and intensities derived from a full solution to the nuclear Hamiltonian [26].

2.5. Density-functional theory (DFT) calculations

The DFT-based full-potential, linearized-augmented plane-wave (FP-LAPW) method as implemented in WIEN2k [27,28] was employed to investigate the competing phase stability of various magnetic configurations in orthorhombic phase of Eu$_2$Sn. For the exchange-correlation functional, a generalized gradient approximation by

Perdew-Burke-Ernzerhof [29] with spin-orbit coupling (SOC) and an onsite electron-correlation (*i.e.*, Hubbard U) parameter [30] were used in all calculations. We used an optimized effective U ($U_{eff} = |U - J|$) of 6.0 eV based on previous theoretical studies on Eu [31]. The core and valence states were treated in a fully relativistic and scalar relativistic manner, respectively. The valence electronic wave functions inside the muffin-tin sphere were expanded up to $l_{max} = 10$. The Brillouin zone integration was performed on sufficiently dense *k*-mesh of $9 \times 13 \times 7$ to achieve total energy (10^{-6} Ry), force, and charge convergence. The optimized value of plane-wave cut-off RK_{max} (=7.0) and G_{max} (= 12.0) with the energy separation of –6.0 Ry between valance and core states were used during the calculation, where K_{max} is largest wave vector basis set.

We note that the magneto-anisotropy energy (MAE) due to SOC is calculated using a global (site-independent) direction of the applied magnetic field H_{field}. Hence, MAE for any sites in a supercell that are non-collinear (*i.e.*, canted with respect to one another) cannot be discerned. Therefore, our DFT results for various MAE orientations are constrained to only collinear cases which nonetheless set the scale of energy (temperature) amongst competing magnetic configurations. We used lattice parameters and atom positions as published for Eu_2Sn in [12].

3. Results and discussion

3.1. Eu_2In

3.1.1. Neutron diffraction

Fig. 1 shows the low-angle region of the thermodiffractogram of Eu_2In, where a diffraction pattern measured at high temperature in the PM state has been subtracted to highlight the purely magnetic scattering intensities.

Four strong magnetic peaks are visible in the shown 2Θ region of the thermodiffractogram which all disappear at about $T_C = 56$ K. Fitting the temperature dependence of the intensity of these magnetic peaks it becomes clear that the magnetic reflection at about $2\Theta = 28°$ has a different temperature dependence (Fig. 2). Contrary to the other reflections, it first increases slowly when going from 2.5 K to 50 K before fading away as well. This can be an indication of a possible different behaviour of the two Eu-sublattices present in the structure as already revealed by the previous Mössbauer studies [12]. The magnetic signal is no longer visible in the data at 56 K.

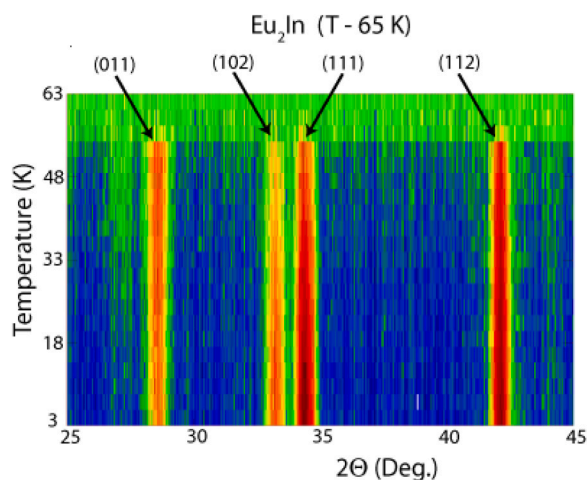A Rietveld refinement of the data at 58 K, in the PM state, was done

Fig. 2. Temperature dependence of selected magnetic peaks of Eu_2In. Error bars are smaller than the symbols. The dashed lines are a guide to the eye.

using the model given in Ref. [16] and is shown in Fig. 3. Lattice parameters at 58 K refined to $a = 7.373(3)$ Å, $b = 5.547(2)$ Å, $c = 10.264$ (4) Å, atom coordinates to Eu1 on 0.037(2), ¼, 0.694(1), Eu2 on 0.171 (2), ¼, 0.070(1) and In on 0.236(3), ¼, 0.394(2). We emphasize that these high intensity but low-resolution data are not intended to serve as a detailed study of the structure but as a basis for the refinement of the magnetic scattering.

Fig. 4a shows the purely magnetic scattering present at 2.5 K created by subtracting the very long measurements taken at 58 K from those measured at 2.5 K. More than 15, partly very intense, magnetic peaks are discernible and were indexed using the program K_Search, which is part of the FULLPROF [21]. suite of programs with the magnetic propagation vector $k = 0$. As the magnetic intensities appear on top of the nuclear peaks, *e.g.*, on top of Bragg peaks allowed in space group *Pnma*, a purely FM structure is indicated.

Magnetic-symmetry analysis was done using the program BASIREPS [22,23] to determine the allowed irreducible representations (IR) and their basis vectors (BV) for the two Eu positions and $k = 0$ in *Pnma*. As the two Eu positions correspond to the same Wyckoff position 4*c* the IRs are identical.

Fig. 1. Thermodiffractogram of Eu_2In showing the angular region having the strongest magnetic reflections. A data set measured at 65 K in the PM region has been subtracted from all data so that the difference data sets contain only the long-range ordered magnetic diffraction intensities.
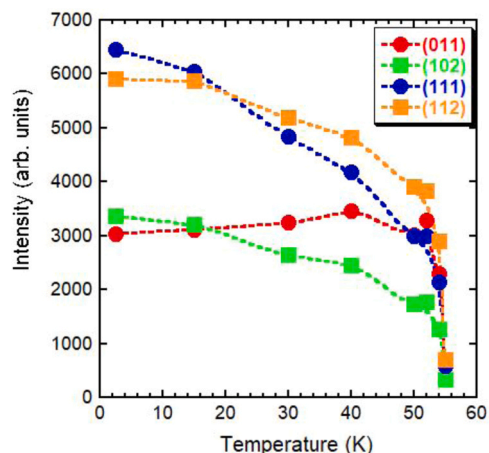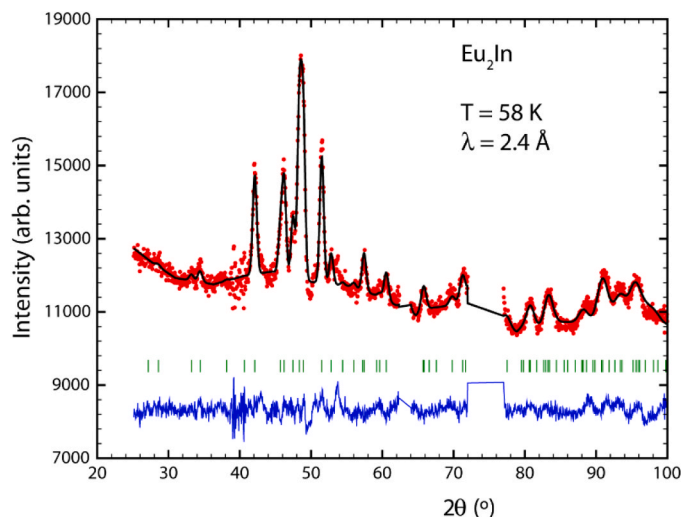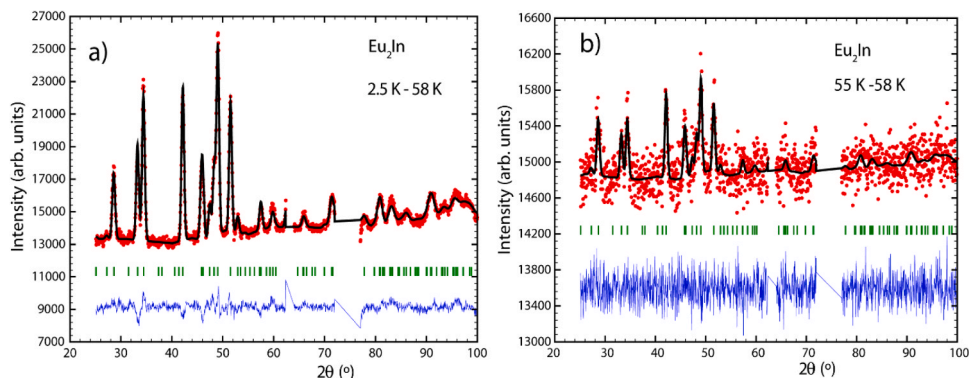

Fig. 3. Observed (red dots), calculated (black line), and difference pattern of the refinement of the nuclear structure of Eu_2In at T = 58 K. The tick marks indicate the calculated positions of reflections in the *Pnma* space group. The excluded region contains strong contributions from the flat Si-plate used to place the thin layer of powdered sample.

Fig. 4. Rietveld refinement fits of the magnetic structure of Eu_2In at (a) 2.5 - 58 K and (b) at 55 - 58 K. Observed intensities are marked as red dots, calculated intensities are marked as black line and their difference as blue line. The tick marks indicate the calculated positions of the magnetic reflections in the *Pnma* space group with $k = 0$. The excluded region contains strong contributions from the flat Si-plate used to place the thin layer of powdered sample.

There are eight allowed IRs having one or two BVs. Three of these IRs have BVs corresponding to a FM alignment of the spins in the unit cell. They were tested against the magnetic intensity and only IR7 can refine the magnetic intensities correctly. This IR corresponds to a FM alignment with spins pointing in direction of the unit cell *a*-direction. The second BV allowed in this IR, which corresponds to an AFM coupling in *c*-direction, does not contribute making the magnetic structure purely FM. The data at T = 2.5 K were first refined directly using a nuclear and a magnetic phase before turning to a refinement of the difference data set 2.5 K - 58 K, where the scale factor, U, V, W and B factor and the zero-shift were fixed to the values found in the refinement of the total data. Data taken at other temperatures were then refined using the corresponding difference data to determine the temperature dependence of the magnetic moments. Two refinements are shown in Fig. 4 for the data at 2.5 - 58 K and at 55 - 58 K, with the latter being the temperature at which the magnetic intensities were visible for the last time. Fig. 4b serves as an example for the advantage of using difference data: the magnetic contribution would have been too low to be accurately determined if the total data at 55 K would have been used for the refinement. The magnetic space group of the magnetic structure of Eu_2In is $Pnm'a'$ (No. 62.447).

As already deduced from the behaviour of the magnetic peaks in the thermodiffractogram, the two Eu sites show a different temperature dependence, as seen in Fig. 5 showing the magnetic moment values *versus* temperature. The values found at 2.5 K for $\mu_{Eu1} = 6.52(3)$ μ_B and $\mu_{Eu2} = 6.81(3)$ μ_B are just slightly below of the 7 μ_B expected for Eu^{2+}
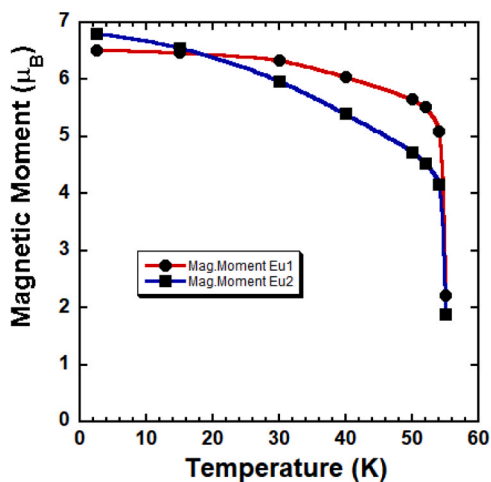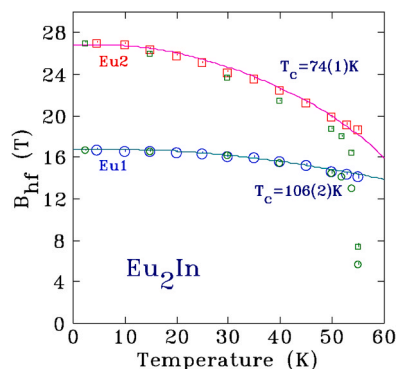
and compare nicely with the values calculated in [5] from DFT.

The magnetic moment values were determined assuming that 100% of Eu is magnetic. As will be shown below, the Mössbauer data indicate the presence of a small and temperature dependent fraction of non-magnetic Eu. Taking this into account the exact value of the magnetic moments on the magnetic Eu^{2+} sites would increase only slightly. Especially at lowest temperature, the determined values are not significantly affected, as the non-magnetic fraction had been determined to about or less 1%. The collapse of the magnetic moments close to T_C supports the interpretation of the magnetic transition being first-order, as already shown from heat-capacity data in [5].

It was not possible to verify the first-order character of the transition using the temperature dependence of the lattice parameters as these high-intensity data have neither the needed angular resolution nor the needed Q-range as the high-angle region is obstructed above $2\Theta \approx 100°$ due to strong scattering from the special sample holder.

3.1.2. Mössbauer spectroscopy

Mössbauer data on Eu_2In and Eu_2Sn have been published before by some of us [12]. Here we present just the temperature dependence of the spectra of Eu_2In re-measured in more detail on a sample originating from the same batch as the one used for the neutron diffraction experiment. The ^{151}Eu Mössbauer spectrum at 5 K for Eu_2In shows two equal area components, consistent with Eu occupying two equal multiplicity crystallographic sites. The fits were done with the two sites constrained to have equal areas, but releasing this constraint did not lead to

Fig. 5. : Plot of magnetic moment values of the two Eu atoms in their corresponding Wyckoff sites as function of temperature.

Fig. 6. : Temperature dependence for the hyperfine fields (B_{hf}) for the two europium sites in Eu_2In. Solid lines are fits using a $J=^7/_2$ mean-field model to estimate the unperturbed ordering temperatures. Also shown, as smaller green symbols, are the magnetic moments taken from Fig. 5, scaled to match at the lowest temperature. The moments and B_{hf} follow the same trend at each site until ≈ 50 K, after which the non-magnetic fraction becomes increasingly significant and the diffraction derived values drop more rapidly.

significant changes in the relative areas. However, the two components have quite different hyperfine fields (B) of 27 T and 17 T (Fig. 6), suggesting that the Eu moments on the two 4c sites are not of the same magnitude. This finding is in accordance with the results of neutron diffraction where moments of 6.8 μ_B and 6.5 μ_B were found. The hyperfine fields also possess quite different temperature dependencies and resemble the temperature dependence of the magnetic moment values, as nicely seen in Fig. 6, where magnetic moments (scaled by a constant so that they match at the lowest temperatures) fall on the same curves as the hyperfine fields. Assuming that the strength of the hyperfine field (not its absolute value), and therefore its temperature dependence, is proportional to the value of the ordered magnetic moment determined by neutron diffraction, it is now possible to assign the component having a hyperfine field of $B_{hf} = 27$ T at 5 K to the Eu2 site and the one having $B_{hf} = 17$ T to the Eu1 site. In [5] it was explained that the FM transition should be triggered by a strong hybridization between Eu-5d and In-5p states. This hybridisation depends on the Eu-In distances, which are different for the two Eu-sites [16], and should explain the different temperature dependences.

Apart from the main signals, there exists a clear non-magnetic component in the Mössbauer spectra. This component grows linearly with temperature (Fig. 7) until very close to the first-order transition, where it diverges. A fit of the spectra without this component is not possible and the feature is too sharp to be magnetic. It can be identified from its isomer shift as Eu^{2+}. The temperature evolution of this non-magnetic component is not reminiscent of the behaviour of an impurity phase which should become non-magnetic at a certain transition temperature and not grow linearly over such a broad temperature range. Also, its fraction exceeds 10% of the total area close to T_C and should therefore show up as an impurity in the diffraction data. A possible origin of this non-magnetic fraction could be a small amount of Eu misplaced on In sites or on interstitial sites that do not order magnetically exactly at T_C but only on further temperature lowering under influence of the surrounding ordered Eu-sublattice network.

The rapid growth of the non-magnetic fraction above ≈ 50 K leads to the scaled neutron diffraction moments deviating below the Mössbauer hyperfine field in Fig. 6. Mössbauer spectroscopy can see the non-magnetic component as distinct from the two magnetic components whereas neutron diffraction can only see the average contribution from each site, and the weighted average of (some moment) and (no moment) leads to an apparent reduction in the fitted moments at both sites. The rounding of the first-order transition seen in the neutron diffraction data (Figs. 5 and 6) is due to the growth of the non-magnetic component, and not to an accelerating reduction in the moments at the two Eu sites.

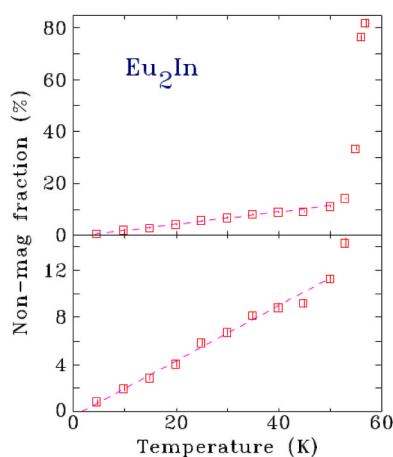We note that phase co-existence is expected and, according to Pecharsky et al. [1] even required for the first-order magnetic phase transitions, where the high-temperature (HT) low-magnetic phase changes to the high-magnetic phase stable at low temperatures (LT). Due to lattice imperfections the first-order transitions in real materials are rarely 100% complete at the transition temperature and the HT phase is sometimes preserved in miniscule quantities much below the T_C [32]. Owing to the negligible lattice differences between HT and LT phases [5] in Eu$_2$In the presence of HT-Eu$_2$In is difficult to observe by powder diffraction. In that regard, our Mössbauer data present the first glance at the existence and magnetic properties of this kinetically arrested phase.

3.2. Eu$_2$Sn

3.2.1. DC magnetic susceptibility

The temperature dependence of the mass magnetic susceptibility $\chi_m(T)$ of Eu$_2$Sn sample measured in applied magnetic fields of H = 0.1, 1, 10, and 50 kOe is presented in Fig. 8. Except for data taken at 100 Oe, the field cooled (FC) data are fully superposed to the ZFC ones, therefore the former were omitted for sake of clarity. $\chi_m(T, 100$ Oe) shows a paramagnetic Curie-like behavior from the room temperature down to ≈ 50 K. Two antiferromagnetic-like cusps appear at ≈ 30 K and 10 K, respectively, in agreement with the neutron diffraction results (see next paragraph). Such cusps broaden and likely merge with increasing applied magnetic field, indicating a field-induced change in magnetic behavior.

In order to extract the Eu-free-ion magnetic moment, we performed a two component Curie-Weiss fit in the range 50–300 K (black line in inset of Fig. 8) by the following model function:

$$\chi_m(T) = w \bullet \frac{C_1}{T} + (1 - w) \bullet \frac{C_2}{T - \theta_2} \qquad (1)$$

Where $w = 0.055$ is the relative weight of the spurious phase Eu$_5$Sn$_3$ as determined by X-ray diffraction data. We neglected the contribution from the other - minor - spurious phase Eu$_2$O$_3$ since in this oxide phase Eu atoms are in the trivalent non-magnetic state. It is worth to note that the actual magnetic properties of Eu$_5$Sn$_3$ are not known. At the same time, we observe that no magnetic transitions occur above 50 K. This leads us to the reasonable assumption of having Eu free-ion paramagnetic behavior also in the spurious Eu$_5$Sn$_3$.

Therefore we safely fixed $C_1 = 0.03534 \frac{cm^3 K}{g}$, the expected value for the Curie constant of Eu$_5$Sn$_3$ for divalent Eu^{2+} free magnetic ions corresponding to an effective magnetic moment of $\mu_{Eu} = 7.94$ μ_B. Thus by fixing the parameters of the impurity phase (w, C_1) we could determine the Curie-Weiss temperature $\theta = +10.1(3)$ K and the Curie constant
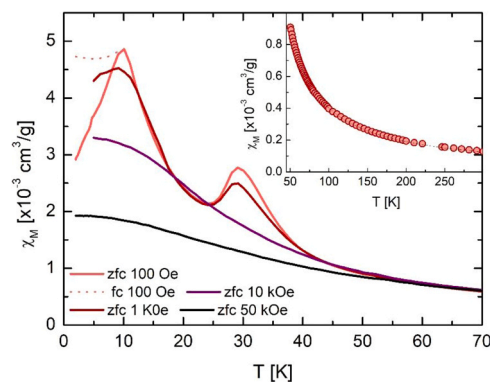

Fig. 7. Trend of the "non-magnetic fraction" as a function of temperature in Eu$_2$In.

Fig. 8. Temperature dependence of the mass magnetic susceptibility χ_m for Eu$_2$Sn as measured with applied magnetic fields of H = 100 Oe, and 1, 10 and 50 kOe. Only data taken with H = 100 Oe present a bifurcation between ZFC-FC curves below the lower transition temperature. Inset: $\chi_m(T)$ measured with an applied magnetic fields of 1 kOe; the black line represents a two component Curie-Weiss fit well above the upper magnetic transition (50 K < T < 300 K). See text for details.

$C_2 = 0.0364(2)\frac{cm^3K}{g}$ for the pure phase. We can argue the following: (i) the Curie-Weiss temperature is positive suggesting the presence of ferromagnetic-like correlations between Eu^{2+} ions, which are prominent in applied magnetic field. (ii) The Curie constant C_2 gives the effective magnetic moment $\mu_{eff} = 7.84(3)$ μ_B for europium ions, in very good agreement with the one expected for divalent europium.

3.2.2. Neutron diffraction

The temperature-dependent neutron-diffraction data of Eu_2Sn confirm the presence of two magnetic transitions as seen in the susceptibility data. The first transition is situated at about 30 K while the second one is found at about 13 K. The two transitions correspond to two different magnetic structures having magnetic peaks at different positions. Fig. 9 shows the magnetic peaks which develop below 30 K; the data correspond to a difference data set where the long measurement taken in the paramagnetic state at 40 K has been subtracted from the long measurement taken at 19.5 K. All magnetic peaks can be indexed with the magnetic propagation vector $k_1 = 0$.

The IRs determined for $k_1 = 0$ by BASIREPS are obviously the same as those obtained for Eu_2In as structure and Eu-positions are the same (Table 1). Again the 8 IRs were tested against the data knowing that in Eu_2Sn the magnetic intensities are appearing at angular positions where no nuclear intensity exists which points to an AFM structure. Only one (IR4) can refine the data: It has only one BV and couples the 4 Eu sites created through the symmetry operations of the $4c$ Wyckoff position antiferromagnetically in b-direction. This is different from the $k = 0$ magnetic structure of the Eu_2In where the coupling was purely ferromagnetic along the a-direction. Although the two Eu $4c$ sites see the same coupling, they have, however, different magnetic moment values. While the Eu1 site on $x = 0.02$, $y = \frac{1}{4}$, $z = 0.69$ has a magnetic moment of ≈ 5 μ_B at 19.5 K, the Eu2 on $x = 0.19$, $y = \frac{1}{4}$, $z = 0.08$ exhibits -3.7 μ_B; the magnetic space group is $Pnma'$ (space group 62.445). The refinement of the difference dataset 19.5 K – 40 K + 15000 represents the situation where only the $k_1 = 0$ type magnetic order exists is shown in Fig. 9. The scale factor used for the refinement of the purely magnetic scattering was obtained by refinement of the nuclear structure from the 40 K data, where the system is in the paramagnetic state. The corresponding magnetic structure is shown in Fig. 10.

The second transition is accompanied by a decrease of the magnetic peaks of the $k_1 = 0$ type magnetic structure; however, their intensity does not go to zero at lowest temperature. This behaviour can be seen in Fig. 11 which displays a low-angle part of the thermodiffractogram of Eu_2Sn where a high-temperature dataset has again been subtracted to show only the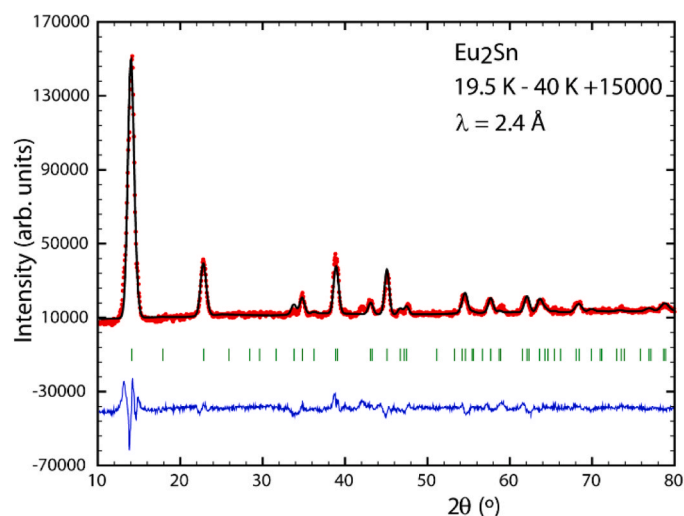 ordered magnetic diffraction intensities. The two reflections visible correspond to the most intense ones of each type of magnetic structure and are closely positioned in 2θ.

While the (001) reflection at $2\Theta = 14°$ is characteristic for the $k_1 = 0$ magnetic structure, which appears at ≈ 30 K, the $(000)^{+k2}$ reflection is characteristic for the magnetic structure appearing at ≈ 13 K. Fig. 12 shows that the integrated intensity of the two reflections where one can see that the k_1 structure starts to decrease at about 13 K but is still present at a significant level at base temperature.

Excluding the magnetic peaks of the k_1 phase the new magnetic peaks appearing below $T_{N2} = 13$ K can be indexed with $k_2 = [0, \frac{1}{2}, \frac{1}{2}]$. The low-temperature data measured at 2.5 K have therefore to be refined using the presence of two coexisting magnetic phases. As often, it is not possible to decide whether they correspond to different parts of the sample volume or whether both are present at the same time as a superposition [33,34]. The goodness of the refinements will be identical. The only way to exclude one or the other is by looking at the values of the magnetic moments resulting from the corresponding refinements. In our case, however, neither of the two possibilities can be excluded this way as shown below. As already mentioned above, the first coupling still corresponds to the AFM model present at 19.5 K with $k_1 = 0$. For the second one, with $k_2 = [0, \frac{1}{2}, \frac{1}{2}]$, BASIREPS gives for this propagation vector 2 IRs with each 6 BVs (Table 2).

Testing all possible combinations of these basis vectors one finds that only IR2 can - with the use of 4 BVs - refine the new magnetic reflections of the k_2 phase appearing below $T_{N2} = 13$ K. Each of the 4 used BVs acts only on 2 atom positions with BV5 =BV2 and BV6 =BV3 coupled to the same value. There are no components pointing in direction of the unit cell b-direction (BV1 = BV4 = 0).

As the BVs of the k_2 structure concern only a- and c-directions and the magnetic contribution coming from the k_1 structure points in b-direction, one can simply superpose both magnetic couplings in a single magnetic phase which embraces the total sample volume. Fig. 13 shows the refinement of the difference data 2.5 K - 40 K using this model which leads to total magnetic moment values at 2.5 K of about 6.6 μ_B for the Eu1 site and 5.1 μ_B for the Eu2 site. These are normal values for Eu^{2+} and this solution is therefore viable. Fig. 14 shows the resulting total magnetic structure where the k_1 and k_2 couplings are superimposed.

If, on the other hand, one assumes a phase separation with one part of the sample volume adopting the k_1 type structure and the other part the k_2 type structure, one has to oblige the magnetic moment values to be the same in both parts to be able to determine phase fractions. As already mentioned above, the data are in this way (using two separated magnetic phases) necessarily refined equally well and returns phase fractions of about $\frac{1}{3}$ for the $k_1 = 0$ phase and about $\frac{2}{3}$ for the $k_2 = [0, \frac{1}{2}, \frac{1}{2}]$ phase. A picture of the k_2 phase is displayed in Fig. 15; its magnetic space group is P_a2_1/c (No. 14.80). Magnetic moment values of $\mu_{Eu1} = 6.6(1)$ μ_B and $\mu_{Eu2} = 5.1(1)$ μ_B are obtained. Different local environments of Eu1 and Eu2 can be put forward to explain the different magnetic moment sizes. While Eu1 possesses five Eu1-Sn bonds one of the five Eu2-Sn bonds is de facto broken as its length reaches nearly 4.5 Å [12]. A surprisingly small value of the hyperfine field of Eu had been found in Eu_2Sn [12] and lead to the question whether the ordered magnetic moment was of the order of 7 μ_B as expected for Eu^{2+}. The results from neutron diffraction show that the magnetic moments are not very far from the expected size and not reduced due to, *e.g.*, low-lying excited crystal-field levels.

We recall here that the refinements do not give any means to decide between the two options and as both solutions lead to acceptable magnetic moment values one must search for other arguments to favour one over the other. In our case it is possible to discuss the behaviour of the k_1 phase as function of temperature: In the solution where both magnetic structures are superposed the magnetic component pointing in b-direction which represents the k_1 coupling is at 2.5 K of the order of 3.5 μ_B for the Eu1 site and of 2.8 μ_B for the Eu2 site. This means that the strength of this coupling has decreased significantly from 5.0 μ_B and 3.7 μ_B

Fig. 9. Refinement of the difference dataset 19.5 K – 40 K + 15000 representing the situation where only the $k_1 = 0$ type magnetic order exists.

Table 1

Allowed irreducible representations (IR) and their basis vectors (BV) for two Eu positions on 4c for $k = 0$ in Pnma. Highlighted in black and red are the IR and the BVs which were used in the refinements of Eu_2In and Eu_2Sn, respectively.

	IR1	IR2		IR3		**IR4**	IR5	IR6		**IR7**		IR8
	BV	BV1	BV2	BV1	BV2	**BV**	BV	BV1	BV2	**BV1**	BV2	BV
x,y,z	0 1 0	1 0 0	0 0 1	1 0 0	0 0 1	**0 1 0**	0 1 0	1 0 0	0 0 1	**1 0 0**	0 0 1	0 1 0
$x+½,-y+½,-z+½$	0 -1 0	1 0 0	0 0 -1	-1 0 0	0 0 1	**0 1 0**	0 1 0	-1 0 0	0 0 1	**1 0 0**	0 0 -1	0 -1 0
$-x,y+½,-z$	0 1 0	-1 0 0	0 0 -1	1 0 0	0 0 1	**0 -1 0**	0 1 0	-1 0 0	0 0 -1	**1 0 0**	0 0 1	0 -1 0
$-x+½,-y,z+½$	0 -1 0	-1 0 0	0 0 1	-1 0 0	0 0 1	**0 -1 0**	0 1 0	1 0 0	0 0 -1	**1 0 0**	0 0 -1	0 1 0
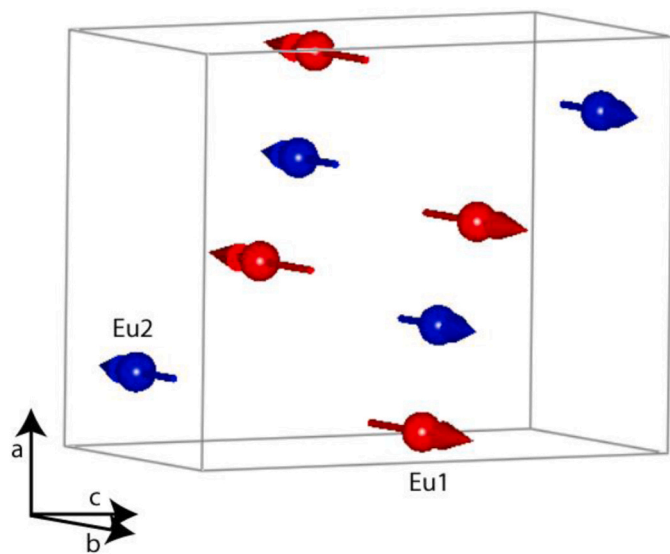
Fig. 10. Experimentally assigned magnetic structure of Eu_2Sn between T_{N1} = 30 K and T_{N2} = 13 K.

determined from the data at 19.5 K. The decrease becomes even more appreciable when refining data taken - with less statistics but still of good quality - just above T_{N2} which show that at T = 13 K the magnetic moments have reached values of μ_{Eu1} = 5.5(1) μ_B and μ_{Eu2} = 4.4(1) μ_B. It seems improbable that the appearance of a new magnetic coupling determined by a different propagation vector should lead on the one hand side to a strong decrease in the strength of the original coupling but

at the same time preserve its persistence down to lowest temperatures. The scenario of a phase coexistence, where different parts of the volume of the sample adopt different magnetic structures, is not so rare [35–40] and has recently been observed in a different Eu-based compound, namely $EuPdSn_2$ [41].

3.2.3. DFT results for Eu_2Sn

The formation energies E_{form} of Eu_2Sn were calculated by DFT to obtain the relative thermodynamic stability of several antiferromagnetic (AFM) configurations and a ferromagnetic (collinear) configuration. E_{form} per atom was calculated using the expression:

$$E_{form} = E_{total} - [2\, E_{Eu} + E_{Sn}] \tag{1}$$

where E_{total} is the total energy of Eu_2Sn in selected magnetic configurations relative to chemical potentials (E_{Eu}, E_{Sn}) of constituent elements. The theoretical simulated structures: (a) AFM-0; (b) AFM-1; (c) AFM-2; (d) AFM-3; (e) AFM-4; are anti-ferromagnetic arrangements of Eu1 and Eu2 sites in the primitive unit cell, where the spins are made as per notation (1 2 3 4), and (1′ 2′ 3′ 4′) exemplified in Fig. 16a, with spin directions given in Table 3. The AFM-1 structure represents an arrangement of Eu moments in a $1 \times 2 \times 2$ orthorhombic supercell designed to simulate configurations based on magnetic propagation vectors, i.e., $k_2 = [0, ½, ½]$ observed experimentally by neutron diffraction (Section 3.2.2), where the periodicity of k_2 indicates a cell twice that of vector [011]. The DFT E_{form} calculated (Table 3) are provided for various magnetic modelled configurations of Eu1 and Eu2 using Eu_2Sn unit cell (per f.u., having 12 atoms per primitive cell). Our stability analysis reveals that all AFM configurations are lower in energy relative to the ferromagnetic (FM) state. Among all AFM cases in Table 3, the lowest-energy configuration is found to be AFM-0 (most stable), i.e., lower than AFM-1 by 4.37 meV/f.u., and FM by 92.65 meV/
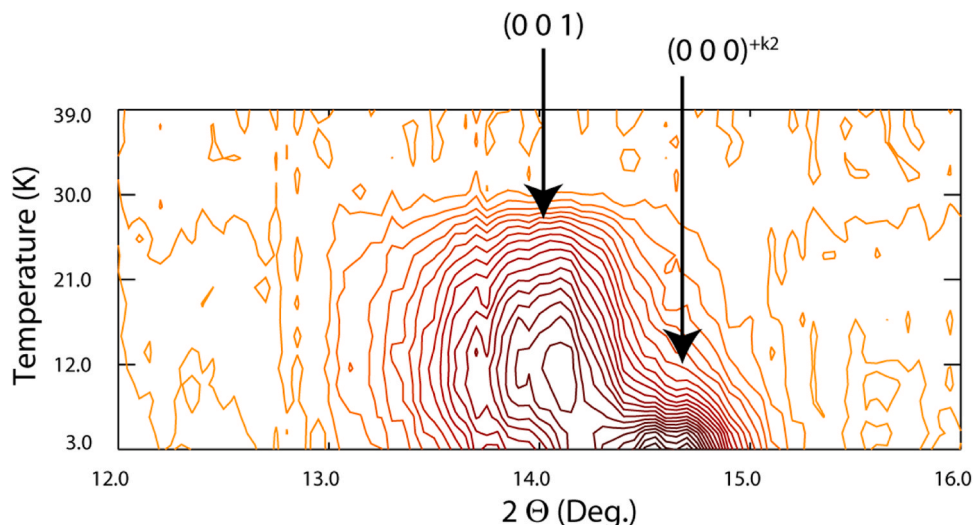
Fig. 11. Thermodiffractogram of Eu_2Sn between 3 K and 39 K and from $12.0° \leq 2\theta \leq 16.0°$.

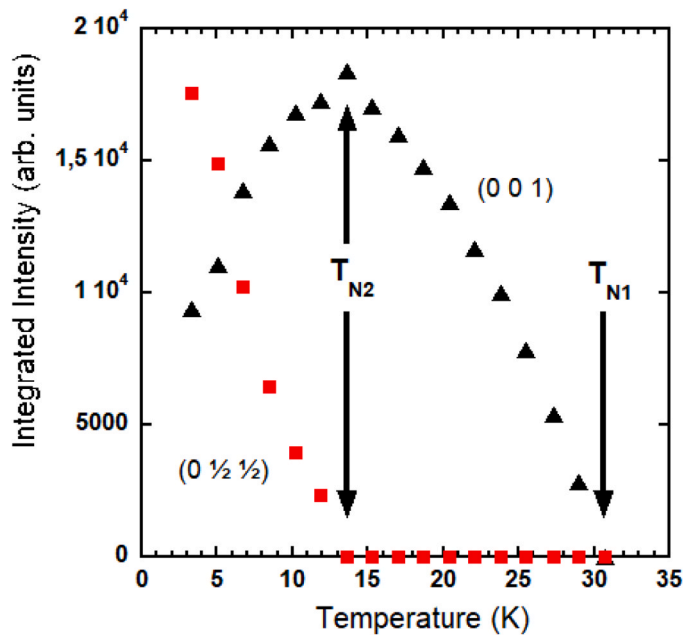**Fig. 12.** Integrated intensities as a function of temperature of the (001) peak representing the $k_1 = 0$ type magnetic structure and of the (0½½) reflection that appears through the $k_2 = [0,½,½]$ type magnetic order.

f.u. Like experiments, the lowest-energy DFT configurations are AFM-0 followed by AFM-1, similar to structures k_1 (Fig. 10) and k_2 (Fig. 15), respectively.

After determining that AFM-0, followed by AFM-1, are the DFT-optimal states, we explored which spin orientations have the lowest energy, given by the magneto-anisotropy energy (MAE) arising from the spin-orbit coupling (SOC). The experimentally observed non-collinearity of low-temperature spin configurations in Eu$_2$Sn (Figs. 14, 15) suggests investigating the SOC effect in high-symmetry directions for all AFM configurations. A detailed energy comparison of the two most stable AFM-0 and AFM-1 arrangements in H$_{field}$ is shown in Table 4. Indeed, the DFT ground-state magnetic orientation for Eu$_2$Sn compound in H$_{field}$ is along (100), with (110) and (010) directions having a very low-energy excitation above - within magnitude of ≈ 0.6 and ≈ 0.2 meV/f.u. for AFM-0 and AFM-1 structures, respectively, so nearly degenerate.

The AFM-0 structure with spins along the (010) direction was experimentally observed above $T_{N2} = 13$ K, so it is not surprising that it was not the DFT ground-state (see Table 3, temperature scale). The DFT energies of AFM-0 are in the order (100) first, (110) second, and (010) third and within ≈ 7 K close to each other, as well as to the rest of the AFM-0 structures (the energetically highest orientation (001) is ≈ 13 K above). In the AFM-1 supercell, the energies for (010) first, (110) second, and (100) third are within 0.2 meV/f.u. The closeness of the results

from the DFT calculations for the AFM-0 and the different AFM-1 models does not allow to decide whether one has a phase coexistence of 2 differently ordered phases or a magnetic structure where AFM-0 and AFM-1 are superposed. Overall, theoretical calculations suggest (100) as the easy magnetic axis for AFM-0 (k_1 structure) and (010) for the AFM-1 (k_2 structure), although in the latter case the difference between (010) and observed (100) is insignificant.

Finally, for a qualitative understanding of bonding in Eu$_2$Sn, we analysed the spatially resolved charge-density difference ($\Delta\rho_{(100-001)}^{charge}$ in Fig. 17b) for the experimentally observed spin configurations, see Table 3. The reoriented charge density lobes at Eu1, Eu2 sites and Sn sites show the effect from spin rearrangement in two distinct planes, *i.e.*, {100}, {001} with a resultant non-collinearity along {110}, the second-most stable configuration (Table 4) of Eu$_2$Sn in AFM-0 (Fig. 17). A closer look at $\Delta\rho_{(100-001)}^{charge}$ reveals that larger charge-density lobes are present at Eu1 sites (more localized charge states) compared to Eu2 sites (less localized charge states), reflecting stronger Eu1-Sn bonding. Additionally, the smaller lobes around Sn atoms also oriented towards Eu1 sites which further support stronger Eu1-Sn bonding. This insight of charge loss due to varying degree of Eu1/Eu2-Sn coupling corroborates well with the reduced averaged moments observed in neutron-diffraction experiments for Eu1 sites ($+5$ μ_B) as compared to Eu2 sites (-3.7 μ_B).

4. Summary and conclusions

Neutron diffraction was used to reveal the magnetic structures in Eu$_2$In and Eu$_2$Sn, where the first compound possesses a first-order transition and a giant magnetocaloric effect [5]. As shown here, the magnetic structures adopted in these two compounds are fundamentally different. While the giant magnetocaloric Eu$_2$In has a simple
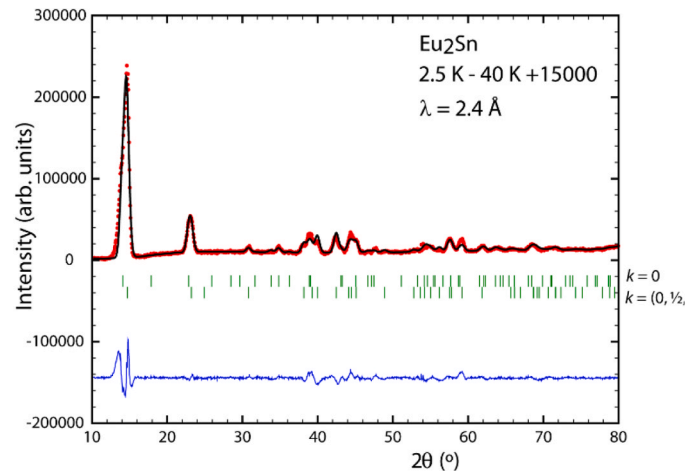

Fig. 13. Refinement of the difference data 2.5 K - 40 K.

Table 2
Allowed irreducible representations (IR) and their basis vectors (BV) for the two Eu (4c) positions for $k_2 = [0, ½, ½]$ in *Pnma*. Highlighted are BVs (black and red) which were coupled in refinements, respectively.

	IR1						IR2					
	BV1	BV2	BV3	BV4	BV5	BV6	BV1	BV2	BV3	BV4	BV5	BV6
x,y,z	0 1 0	0 0 0	0 0 0	0 0 0	1 0 0	0 0 1	0 1 0	0 0 0	0 0 0	0 0 0	**1 0 0**	**0 0 1**
x+½,-y+½,-z+½	0 -1 0	0 0 0	0 0 0	0 0 0	1 0 0	0 0 -1	0 1 0	0 0 0	0 0 0	0 0 0	**-1 0 0**	**0 0 1**
-x,y+½,-z	0 0 0	1 0 0	0 0 1	0 1 0	0 0 0	0 0 0	0 0 0	**-1 0 0**	**0 0 -1**	0 -1 0	0 0 0	0 0 0
-x+½,-y,z+½	0 0 0	1 0 0	0 0 -1	0 -1 0	0 0 0	0 0 0	0 0 0	**1 0 0**	**0 0 -1**	0 -1 0	0 0 0	0 0 0

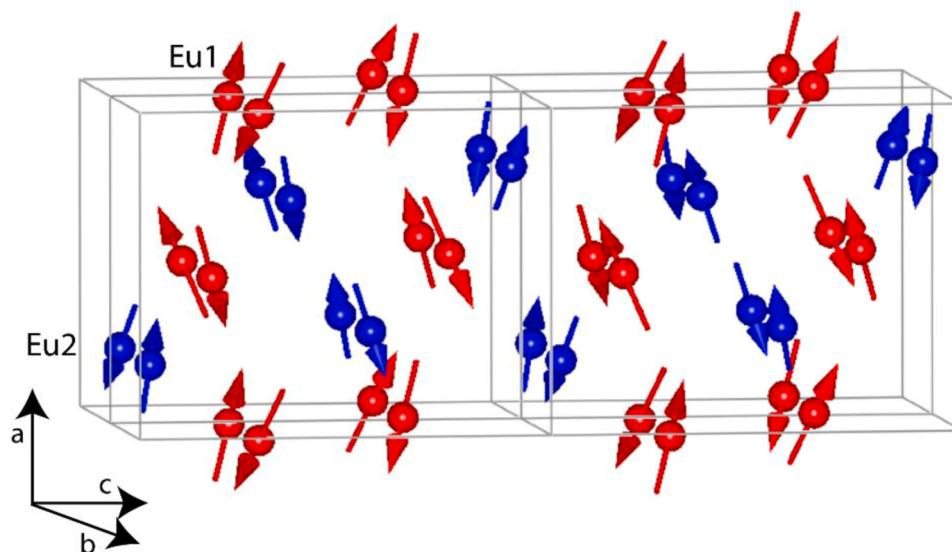**Fig. 14.** Total magnetic structure of Eu$_2$Sn assuming a superposition of k_1 and k_2 couplings throughout the whole sample volume (below T$_{N2}$ = 13 K).

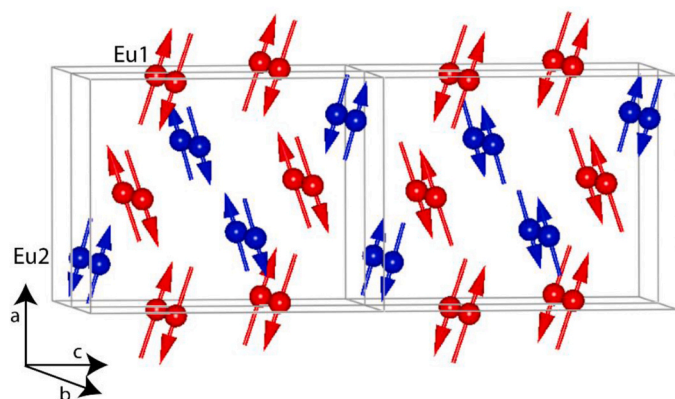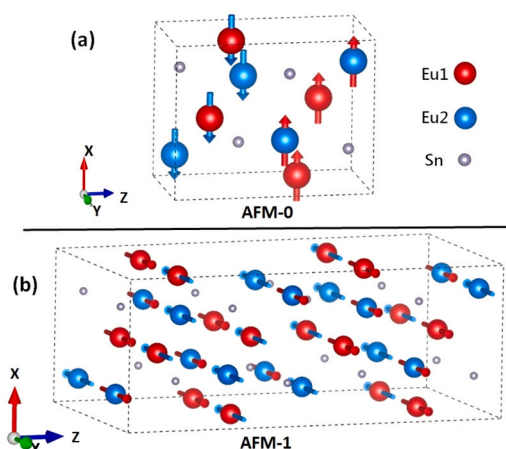**Fig. 15.** Magnetic structure of the k_2 phase in Eu$_2$Sn (below T$_{N2}$ = 13 K).

Fig. 16. AFM arrangements calculated along **H**$_{field}$ to assess Eu$_2$Sn ground-state, the (a) AFM-0 structure (*most stable*), where Eu1 sites [denoted by (1 2 3 4)] and Eu2 sites [denoted by (1′ 2′ 3′ 4′)] are given in Table 3 with a = 7.84 Å, b = 5.41 Å, and c = 9.913 Å having orthorhombic (*Pnma*) cell; and (b) AFM-1 structure (*next-most stable* with $1 \times 2 \times 2$ supercell), as in Table 4, the alignment along b-axis (*i.e.*, y-direction) is higher by only 0.2 meV/f.u., roughly the MAE between b and a axes.

Table 3

DFT E_{form} of selected Eu$_2$Sn magnetic configurations. Except AFM-1, the moment orientations of Eu1 and Eu2 sites (Fig. 16a) with respect to the conventional c-axis (no SOC) are marked by up/down arrows. The most stable orientation for AFM-1 structure is shown in Fig. 16b. Second to last column shows the difference ΔE_{form} relative to AFM-0 configuration.

Magnetic configuration	Eu1 (1 2 3 4)	Eu2 (1′ 2′ 3′ 4′)	E_{form} [eV/f.u.]	ΔE_{form} [meV/f.u.]	Difference ΔE_{form} [meV/atom K]
AFM-0	↓↓↑↑	↓↓↑↑	− 7.825	0	0 (0 K)
AFM-1	See Fig. 16b		− 7.8205	+ 4.37	0.364 (4.2 K)
AFM-2	↑↓↓↑	↓↑↑↓	− 7.7835	+ 41.49	3.46
AFM-3	↑↓↓↑	↑↓↓↑	− 7.754	+ 70.92	5.91
AFM-4	↑↑↑↑	↓↓↓↓	− 7.742	+ 83.22	6.94
FM	↑↑↑↑	↑↑↑↑	− 7.732	+ 92.65	7.72

Table 4

For global H$_{field}$ direction (which reorients spins against MAE due to SOC), we report our *constrained* DFT energy difference (MAE = $E_{(H)} - E_{(min)}$) for orientations relative to the lowest-energy direction in AFM-0 and AFM-1 from Table 3. The stars " * " indicate the orientations observed experimentally. For the k_1 = 0 magnetic structure it lies ≈ 7 K above the DFT calculated ground-state AFM-0 along (100). The experimentally observed $k_2 = [0, ½, ½]$ magnetic structure is canted by about 20° towards the (001) direction but points mainly in the (100) direction. Its orientation is therefore ≈ 2.3 K above the DFT calculated ground-state AFM-1 along (010).

H$_{field}$	AFM-0 $E - E_{(100)}$ [meV/f.u.]	AFM-1 $E - E_{(010)}$ [meV/f.u.]
100	**0**	0.199 *
110	0.518	0.063
010	0.618*	**0**
021	*n/a*	0.087
111	0.638	0.341
101	0.807	0.647
011	0.796	0.365
012	*n/a*	0.532
001	1.097	0.719

ferromagnetic structure, Eu$_2$Sn orders antiferromagnetically and sees the presence of two magnetic propagation vectors appearing at two different magnetic transitions. The different temperature dependencies of the magnetic moment values of the two different Eu sites in Eu$_2$In can
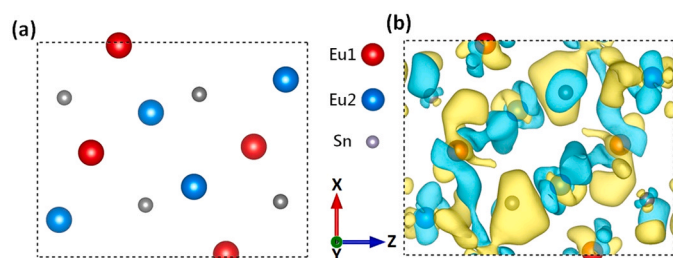
Fig. 17. (a) Projection of the Eu_2Sn atomic structure on the x-z plane; (b) charge-density difference ($\Delta\rho^{charge}_{(100-001)}$) calculated for spin configurations arranged according to theoretical stable (close to k_1 experimental) structure. Iso-surfaces of 1.5×10^{-5} $e/a.u.^3$ were used to fit charge density. Charge density gain (loss) shown by yellow (blue) contours.

be nicely scaled to the T-dependence of the Mössbauer hyperfine field data. Differences in the local environments of Eu_2In and Eu_2Sn have been pointed out in [12] and should be responsible for the different magnetic structures adopted. While the magnetic interactions in Eu_2In are influenced by conduction electrons, which are likely responsible for the first-order transition [5,12,13], Eu_2Sn has traditional RKKY-type mediated exchange, which is supported by the agreement of our DFT calculations, where $4f$ electrons were treated as core, with the experiment. The DFT results clearly exclude the FM state for Eu_2Sn, in distinction to what had been found for Eu_2In [5,13,14]. They suggest furthermore the energetic proximity of competing magnetic configurations, and corroborate the essential finding of the experimental analysis, with Eu_2Sn having two Eu-sites antiferromagnetically ordered.

Declaration of Competing Interest

The authors declare that they have no known competing financial interests or personal relationships that could have appeared to influence the work reported in this paper.

Data Availability

Data will be made available on request.

Acknowledgements

References

[1] V.K. Pecharsky, K.A. Gschneidner Jr., Y. Mudryk, D. Paudyal, J. Magn. Magn. Mater. 321 (2009) 3541–3547.
[2] J. Liu, T. Gottschall, K.P. Skokov, J.D. Moore, O. Gutfleisch, Nat. Mater. 11 (2012) 620–626.
[3] X. Moya, S. Kar-Narayan, N.D. Mathur, Nat. Mater. 13 (2014) 439–450.
[4] J.Y. Law, L.M. Moreno-Ramirez, A. Diaz-Garcia, V. Franco, J. Appl. Phys. 133 (2023) 1–13, 040903.
[5] F. Guillou, A.K. Pathak, D. Paudyal, Y. Mudryk, F. Wilhelm, A. Rogalev, V. K. Pecharsky, Nat. Commun. 9 (2018) 1–9, 2925.
[6] F. Guillou, H. Yibole, R. Hamane, V. Hardy, Y.B. Sun, J.J. Zhao, Y. Mudryk, V. K. Pecharsky, Phys. Rev. Mater. 4 (2020) 1–9, 104402.
[7] Y. Yu, R. Liu, L. Zhang, G. Yao, Q. Wang, J. Zhu, S. Yang, W. Cui, J. Magn. Magn. Mater. 524 (2021) 1–5, 167648.
[8] W. Liu, F. Scheibel, T. Gottschall, E. Bykov, I. Dirba, K. Skokov, O. Gutfleisch, Appl. Phys. Lett. 119 (2021) 1–6, 022408.
[9] W. Cui, G. Yao, S. Sun, Q. Wang, J. Zhu, S. Yang, J. Mater. Sci. Technol. 101 (2022) 80–84.
[10] A. Biswas, R.K. Chouhan, A. Thayer, Y. Mudryk, I.Z. Hlova, O. Dolotko, V. K. Pecharsky, Phys. Rev. Mater. 6 (2022) 1–11, 114406.
[11] B. Liu, G. Zeng, G. Yao, S. Yang, Q. Wang, W. Cui, J. Magn. Magn. Mater. 568 (2023) 1–5, 170409.
[12] D.H. Ryan, D. Paudyal, F. Guillou, Y. Mudryk, A.K. Pathak, V.K. Pecharsky, AIP Adv. 9 (2019) 1–4, 125137.
[13] E. Mendive-Tapia, D. Paudyal, L. Petit, J.B. Staunton, Phys. Rev. B 101 (2020) 1–7, 174437.
[14] B.P. Alho, P.O. Ribeiro, P.J. von Ranke, F. Guillou, Y. Mudryk, V.K. Pecharsky, Phys. Rev. B 102 (2020) 1–6, 134425.
[15] J. Flahaut, F. Thevet, J. Solid State Chem. 32 (1980) 365–376.
[16] M.L. Fornasini, S. Cirafici, Z. Kristallogr. 190, 1990, pp. 295–304.
[17] A. Palenzona, P. Manfrinetti, M.L. Fornasini, J. Alloy. Compd. 280 (1998) 211–214.
[18] Materials Preparation Center, The Ames Laboratory, US Department of Energy, Ames, IA, USA, www.mpc.ameslab.gov.
[19] K. Yvon, W. Jeitschko, E. Parthé, J. Appl. Cryst. 10 (1977) 73–74.
[20] J. Rodriguez-Carvajal, L.M.D. Cranswick, J. Appl. Cryst. 41 (2008) 198–205.
[21] J. Rodriguez-Carvajal, Phys. B 192 (1993) 55–69.
[22] J. Rodriguez-Carvajal, BASIREPS: a program for calculating irreducible representations of space groups and basis-functions for axial and polar vector properties; Part of the FullProf Suite of programs available at: www.ill.eu/sites/fullprof/.
[23] C. Ritter, Solid State Phenom. 170 (2011) 263–269.
[24] J.M. Perez-Mato, S.V. Gallego, E.S. Tasci, L. Elcoro, G. de la Flor, M.I. Aroyo, Annu. Rev. Matter Res. 45 (2015) 217–248.
[25] M.I. Aroyo, J.M. Perez-Mato, C. Capillas, E. Kroumova, S. Ivantchev, G. Madariaga, A. Kirov, H. Wondratschek, Z. Krist. —Cryst. Mater. 221 (2006) 15–27.
[26] C.J. Voyer, D.H. Ryan, Hyperfine Inter. 170 (2006) 91–104.
[27] P. Blaha, K. Schwarz, G. Madsen, D. Kvasnicka, J. Luitz, WIEN2k: An Augmented Plane Wave Plus Local Orbitals Program for Calculating Crystal Properties. ISBN 3–9501031-1–2 (2001).
[28] P. Blaha, K. Schwarz, F. Tran, R. Laskowski, G.K.H. Madsen, L.D. Marks, J. Chem. Phys. 152 (2020) 1–30, 074101.
[29] J.P. Perdew, K. Burke, M. Ernzerhof, Phys. Rev. Lett. 77 (1996) 3865–3868.
[30] S.L. Dudarev, G.A. Botton, S.Y. Savrasov, C.J. Humphreys, A.P. Sutton, Phys. Rev. B 57 (1998) 1505–1509.
[31] S. Muñoz Pérez, R. Cobas, J.M. Cadogan, J. Albino Aguiar, S.V. Streltsov, J. Appl. Phys. 117 (2015) 1–4, 17C702.
[32] Y. Mudryk, A.P. Holm, K.A. Gschneidner Jr, V.K. Pecharsky, Phys. Rev. B 72 (2005) 1–11, 064442.
[33] M. Smidman, C. Ritter, D.T. Adroja, S. Rayaprol, T. Basu, E.V. Sampathkumaran, A. D. Hillier, Phys. Rev. B 100 (2019) 1–8, 134423.
[34] C. Ritter, S. Sharma, D.T. Adroja, Phys. Rev. Mat. 6 (2022) 084405 (1_12).
[35] C. Ritter, R. Mahendiran, M.R. Ibarra, L. Morellon, A. Maignan, B. Raveau, C.N. R. Rao, Phys. Rev. B 61 (2000). R9229-R9232.
[36] M. Respaud, J.M. Broto, H. Rakoto, J. Vanacken, P. Wagner, C. Martin, A. Maignan, B. Raveau, Phys. Rev. B 63 (2001) 1–6, 144426.
[37] W. Westerburg, O. Lang, C. Ritter, C. Felser, W. Tremel, G. Jakob, Sol. State Comm. 122 (2002) 201–206.
[38] C. Ritter, S.A. Ivanov, G.V. Bazuev, F. Fauth, Phys. Rev. B 93 (2016) 1–11, 054423.
[39] K.H. Hong, A.M. Arevalo-Lopez, J. Cumby, C. Ritter, J.P. Attfield, Nat. Comm. 9 (1-6) (2018) 2975.
[40] S. Rayaprol, V. Siruguri, A. Hoser, C. Ritter, E.V. Sampathkumaran, Phys. Rev. B 90 (2014) 1–7, 134417.
[41] A. Martinelli, D. Ryan, J. Sereni, C. Ritter, A. Leineweber, I. Curlık, R. Freccero, M. Giovannini, J. Mater. Chem. C. 11 (2023) 7641–7653.